Dynamic coupling of mass transfer and chemical reaction for Taylor flow along a serpentine microchannel

Journal:	*Industrial & Engineering Chemistry Research*
Manuscript ID	ie-2020-00014t.R4
Manuscript Type:	Article
Date Submitted by the Author:	21-Apr-2020
Complete List of Authors:	zhou, yufei; Yantai University, College of Chemistry & Chemical Engineering Yao, Chaoqun; Chinese Acad Sci Zhang, Peng; Yantai University Zhang, Xunli; University of Southampton, School of Engineering Lü, Hongying; College of Chemistry and Chemical Engineering, Yantai University, Zhao, Yuchao; Yantai University, College of Chemistry & Chemical Engineering

SCHOLARONE™
Manuscripts

Dynamic coupling of mass transfer and chemical reaction for Taylor flow along a serpentine microchannel

Yufei Zhou[a,ξ], Chaoqun Yao[b,ξ], Peng Zhang[a], Xunli Zhang[c], Hongying Lü[a], Yuchao Zhao[a,*]

[a] Shandong Collaborative Innovation Center of Light hydrocarbon transformation and utilization, School of Chemistry & Chemical Engineering, Yantai University, Yantai 264005, China

[b] Dalian National Laboratory for Clean Energy, Dalian Institute of Chemical Physics, Chinese Academy of Sciences, Dalian116023, China

[c] School of Engineering & Institute for Life Sciences, University of Southampton, Southampton SO17 1BJ, UK

[ξ] The authors contribute equally to the paper

ABSTRACT

The characteristics of multiphase dynamic mass transfer play a big role in gaining understanding and controllability of gas-liquid two-phase chemical absorption processes. In the present work, dynamic coupling of mass transfer and chemical reaction for Taylor flow in a serpentine microchannel was investigated by an online method. The dynamic changes of gas bubbles, key mass transfer parameters (i.e., $k_L a$, k_L and a) and the enhancement factor were measured and calculated, where three changing stages were found under different operating conditions of Q_G (2-5.5 mL), Q_L (1-2.5 mL), W_{MEA} (1-3 wt%). Based on the experimental results, a modified van Baten's model was proposed to predict mass transfer performance for both CO_2-H_2O and CO_2-MEA systems, and the correlation coefficients were 0.95 and 0.96, respectively. The correlations also suggested the net physical mass transfer performance in CO_2-MEA system could be reasonably separated from the chemical absorption process.

* Corresponding Author. Tel: +86 535 6903386.
  E-mail address: yczhao@ytu.edu.cn (Y. Zhao).

1

1. INTRODUCTION

Among the current technologies for the removal of CO_2, chemical absorption with monoethanolamine (MEA) solution has been the most widely used one.[1,2] Although great efforts have been made to develop gas-liquid contactors for higher process efficiency, the amount of absorbent used, the energy consumption and the equipment investment are still far from satisfactory.[3,4]. Generally, the efficiency of gas-liquid contactors is determined by gas-liquid mass transfer performance, where the dynamic change (e.g., formation, growth, shrinkage, collapse and coalescence) of bubbles plays an important role. Due to the complex hydrodynamics of gas bubble populations, there still remains challenges to measure the instantaneous volumetric mass transfer coefficient with high spatiotemporal precision.[5,6]

In recent years, microchannel contactors have been developed into powerful tools for measuring the volumetric mass transfer coefficient, owing to its small characteristic dimension, large surface-to-volume ratio and controllable gas-liquid flow patterns.[7-14] Berčič and Pintar put forward an empirical correlation based on a unit cell model for predicting the liquid side volumetric mass transfer coefficient (k_La) in methane-water system under Taylor flow; they found that (k_La) was mostly determined by the liquid slug length and velocity.[15] van Baten and Krishna investigated mass transfer from Taylor bubbles to the liquid phase by computational fluid dynamics, and found that k_La was determined by the sum of the contributions of the two bubble caps and the film surrounding the bubble.[16] Yue et al. examined CO_2 absorption in water and $NaHCO_3/Na_2CO_3$ buffer solution, and proposed an improved

2

1   empirical correlation for determining k_La.[17,18] Li et al. studied the effects of flow rates

2   on k_La in Taylor flow with CO_2-MEA system.[19] Recently, Chu et al. investigated

3   experimentally the mass transfer characteristics of CO_2 absorption into aqueous

4   solution of ionic liquid in microchannel and proposed a dimensionless correlation to

5   predicting k_La.[20] In these studies, k_La was generally assumed to be constant across the

6   entire reactor under given operating conditions. However, the dynamic shrinkage of

7   Taylor bubble along the microchannel was disregarded.

8   To address this issue, Cubaud et al. measured the evolution of CO_2 bubble size with

9   physical solvents in long serpentine microchannels by tracking individual bubbles

10   along the flow direction to establish the functional relationship between bubble size

11   and velocity.[21,22] Abolhasani et al. developed an automated microfluidic platform to

12   determine CO_2 solubility, k_La, as well as the reducing rate of Taylor bubbles, which

13   could be translated into mass transfer performance.[23] Similar effort was made by Tan

14   et al. to measure the changes of gas bubble volume versus flowing distance, which

15   was beneficial to further estimation of k_La.[24] By developing a unit cell model, Yao et

16   al. built a relation between k_La and the reducing rate of CO_2 bubbles, realizing direct

17   measurement of k_La through monitoring CO_2 bubbles size.[25] Zhang et al. used a

18   similar model to characterize gas-liquid mass transfer for CO_2-H_2O system.[14]

19   Although these investigations shed considerable light on the dynamic characteristics

20   of the gas-liquid mass transfer process, these findings were limited to physical

21   absorption and differed from chemical absorption processes.

22   There have been efforts made in examining the mass transfer of CO_2 chemical

3

1 absorption into aqueous MEA solutions for Taylor flow along microchannels.[19,26,27]

2 Zhu et al. found the bubble length decreased exponentially along the microchannel

3 due to CO_2 reactive absorption, and a turning point existed in the flowrate ratio of gas

4 and liquid phases for different MEA concentrations[26]. A correlation for predicting $k_L a$

5 was also proposed by integrating the enhancement factor of chemical reaction[27].

6 However, these studies were still limited to treating $k_L a$ as constant. Moreover, the

7 dynamic change of mass transfer enhancement due to chemical reaction was not

8 considered.

9 Based on the above analysis, the aim of the present work was to quantitatively

10 characterize the dynamic coupling of mass transfer and chemical reaction under

11 Taylor flow of the CO_2-MEA system along a microchannel. An online imaging

12 technique with a high-speed camera and a stereo microscope was employed to

13 measure the evolution of the geometry and movement of gas bubbles. The dynamic

14 changes were quantified in terms of $k_L a$, liquid phase mass transfer coefficient (k_L),

15 specific interfacial area (a) and enhancement factor (E). A theoretical model was

16 established for determining E. In order to predict the local mass transfer performance,

17 a model was proposed for both CO_2-H_2O and CO_2-MEA systems. These findings

18 would provide strong foundation for designing and optimizing gas-liquid

19 microchannel contactors towards high process performance.

2. EXPERIMENTAL SECTION

21 The experimental setup is shown schematically in Figure 1(a). Two high pressure

22 syringe pumps (LSP01-1BH, Longer) and two stainless steel syringes (50 mL, Longer)

4

1   were used to deliver gas and liquid, respectively. The gas and liquid flow rates were

2   calibrated by the weighting method and an automated electronic soap film flowmeter

3   (GL-101B, 0.1-100 mL/min, accuracy 1%, Beijing Beifen Sanpu, China), respectively.

4   CO_2 (99.999 vol%) and aqueous MEA solution (analytical grade, Sinopharm

5   Chemical Reagent Co., Ltd.) were used as the working fluids. The operating

6   temperature was set at 25 ^{o}C. The pressure drop across the flow channel was

7   measured by a pressure transducer (DMP305X, 0~50kPa, accuracy 0.075%, LEEG,

8   China). Across the whole length (200 mm) of the microchannel, the overall pressure

9   drop was found to be minimal (< 6.6 kPa) suggesting that the evolution of the local

10   pressure along the microchannel was insignificant. Therefore, a linear correlation was

11   used to represent P_{CO2} as a function X in this work. The concentrations of the aqueous

12   MEA solution were set at four levels, i.e., 1.0, 1.5, 2.0 and 3.0 wt%. The main reason

13   for choosing the MEA concentration range (1.0-3.0 wt%) in this study was to enable

14   practically measuring the gas-liquid mass transfer performance, although it was

15   relatively lower than that in industrial applications. The dynamic changes of CO_2

16   bubbles were recorded by a high-speed camera (Phantom R311, 3200 fps) mounted on

17   a stereo microscope (Olympus SZX 16). The resolution and exposure time were 1280

18   $\times 800$ pixels and 490 μs, respectively.

19

20   (a)   (b)   (c)

5
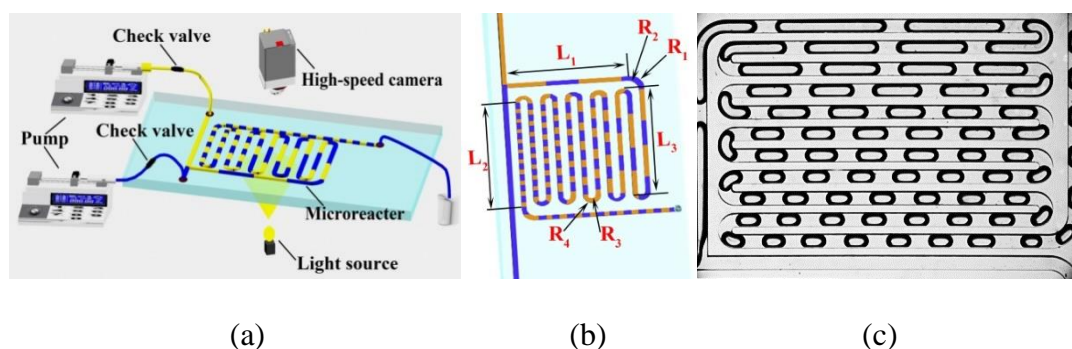
1   **Figure 1.** T-junction microchannel and gas-liquid mass transfer system (a) Schematic

2   of the experimental setup; (b) T-junction microchannel; (c) Typical captured image.

3   Figure 1(b) illustrates the layout design of the microchannel with a T-junction

4   followed by a long serpentine microchannel. The design parameters (width, depth,

5   length, and radius) for different sections of the microchannel are summarized in Table

6   1. The microchannels were fabricated on PMMA plates (A grade, 92% of light

7   transmittance, ShenZhen HuiLi Acrylic Products Co., Ltd.) by precision milling and

8   sealed by thermal sealing. Figure 1(c) shows a snapshot captured by a high-speed

9   camera focused on the main area covering all 12 serpentine microchannels. 1000

10   images were taken from each set of experiment, and the changes in bubble length and

11   velocity along the microchannel were analyzed by Matlab image analysis program.

12   **Table 1.** Geometries (mm) of microchannel in Figure 1(b)

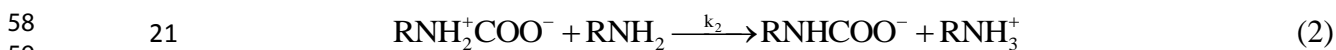| Width/w	Depth/h	L_1	L_2	L_3	R_1	R_2	R_3	R_4	Total length/L
0.6	0.6	9.43	14.28	13.96	1.0	1.5	0.2	0.8	181.13

13   ## 3. PROCESS ANALYSIS AND MODELING

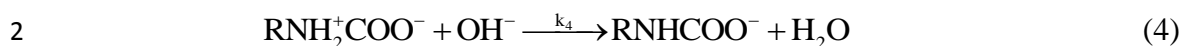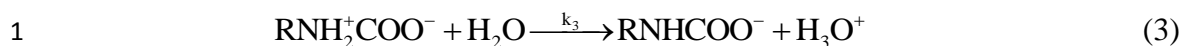14   ### 3.1. Reaction Mechanisms and Mass Transfer Process Analysis

15   The chemical reaction of CO_2 with aqueous MEA solution can be interpreted by

16   either the zwitterion mechanism[28,29] or the termolecular mechanism.[30,31] The former

17   was more commonly used.[32,33]

18   Zwitterion formation:

19

$$CO_2 + RNH_2 \underset{k_{-1}}{\overset{k_1}{\rightleftharpoons}} RNH_2^+COO^-$$ (1)

20   Zwitterion deprotonation:

21

$$RNH_2^+COO^- + RNH_2 \xrightarrow{k_2} RNHCOO^- + RNH_3^+$$ (2)

1    $$RNH_2^+COO^- + H_2O \xrightarrow{\ k_3\ } RNHCOO^- + H_3O^+ \tag{3}$$

2    $$RNH_2^+COO^- + OH^- \xrightarrow{\ k_4\ } RNHCOO^- + H_2O \tag{4}$$

3   where R denotes $-CH_2CH_2OH$.

4   Combining Eqs. (1)-(4), the following expression was obtained based on the

5   assumption of quasi-steady state for the zwitterion concentration.

6    $$r_{CO_2} = \frac{-k_1 C_{CO_2} C_{MEA}}{1 + \dfrac{k_{-1}}{k_2 C_{MEA} + k_3 C_{H_2O} + k_4 C_{OH^-}}} \tag{5}$$

7   Generally, the zwitterion deprotonation was much faster than its decomposition, i.e.,

8    $k_{-1}/\left(k_2 C_{MEA} + k_3 C_{H_2O} + k_4 C_{OH^-}\right) << 1$, then the rate of CO_2 reaction with MEA could

9   be expressed by a simple second-order kinetics[29,34]:

10   $$-r_{CO_2} = k_1 C_{CO_2} C_{MEA} \tag{6}$$

11   where k_1 could be determined by the following empirical correlation:[34]

12   $$\log_{10} k_1 = 10.99 - 2152/T \tag{7}$$

13   The mass balance for CO_2 and MEA in the liquid phase based on two-film model was

14   written in the following,

15   $$\begin{cases} D_{CO_2}\left(\dfrac{d^2 C_{CO_2}}{dz^2}\right) - k_1 C_{CO_2} C_{MEA} = 0 \\[4mm] D_{MEA}\left(\dfrac{d^2 C_{MEA}}{dz^2}\right) - k_1 C_{CO_2} C_{MEA} = 0 \end{cases} \tag{8}$$

16   Boundary conditions,

17   $$z = 0,\ C_{CO_2} = C_{CO_2,i},\ \frac{dC_{MEA}}{dz} = 0;\quad z = \delta,\ C_{CO_2} = 0,\ C_{MEA} = C_{MEA,L} \tag{9}$$

18   where $C_{CO_2,i}$ was CO_2 concentration at the gas-liquid interface, mol/m³; $C_{MEA,L}$ was

7

1　　MEA concentration in the bulk liquid phase, mol/m^3. D_{CO_2} and D_{MEA} were the

2　　diffusion coeffcient of CO_2 and MEA in aqueous MEA solution[35], respectively, m^2/s.

3
$$\ln D_{MEA} = -13.275 - 2198.3/T - 7.8142 \times 10^{-5} C_{MEA} \tag{10}$$

4
$$D_{CO_2} = \left(2.35 + 0.029837 C_{MEA} - 9.7078 \times 10^{-3} C_{MEA}^2\right) \times 10^{-6} \exp\left(\frac{-2119 - 20.132 C_{MEA}}{T}\right) \tag{11}$$

5　　For determining the enhancement factor, E, the analytical solution of van Krevelen

6　　and Hoftijzer was adopted:[36]

7
$$E = \frac{\sqrt{Ha^2 \dfrac{E_\infty - E}{E_\infty - 1}}}{\tanh \sqrt{Ha^2 \dfrac{E_\infty - E}{E_\infty - 1}}} \tag{12}$$

8　　where Ha and E_∞ as Hatta number and the infinite enhancement factor based on

9　　two-film model, respectively, were expressed as,

10
$$Ha = \frac{\sqrt{D_{CO_2} k_1 C_{MEA,L}}}{k_L^0} \tag{13}$$

11
$$E_\infty = 1 + \frac{D_{MEA} C_{MEA,L}}{D_{CO_2} C_{CO_2,i}} \tag{14}$$

12　　where k_L^0 denoted the liquid side physical mass transfer coefficient, m/s.

13

14　　**3.2. Modeling of Mass Transfer Coefficient**

15　　A unit cell model for Taylor flow was used,[14,16,25] as shown in Figure 2(a). There

16　　were a few assumptions associated with the model: (i) CO_2 and aqueous MEA

17　　solution were well-mixed in each phase in a unit cell; (ii) the overall unit cell was

18　　considered as a plug flow; (iii) mass transfer and reaction from CO_2 to aqueous MEA

19　　solution only happened within a unit cell; and (iv) each unit cell was independent.

8
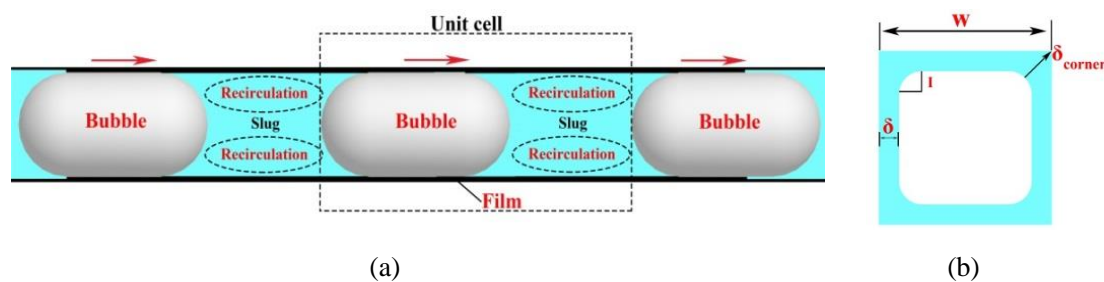
Figure 2. Schematic of typical gas-liquid two-phase Taylor flow in a microchannel. (a) Taylor bubble and slug in a unit cell. (b) Cross-section of Taylor bubble (not to scale).

The mass balance of CO_2 in a unit cell was described as the following.

$$\frac{P_{CO_2}}{RT} \cdot \frac{dV_B}{dX} U_B = -k_L a \left(C_{CO_2}^{*,L} - C_{CO_2}^{L} \right) \left(V_B + V_L \right) \tag{15}$$

where P_{CO_2} was gas phase pressure which varied along the microchannel as a result of local pressure, Pa; R was gas constant, 8.3145 J/(mol·K). T was operating temperature, K; V_B was volume of CO_2 bubble, m^3; U_B was velocity of CO_2 bubble, m/s, varying along the microchannel as a result of mass transfer and reaction; X was position along the serpentine microchannel, m. k_L was liquid phase mass transfer coefficient, m/s. a was specific interfacial area ($a = A_S / (V_{CO_2} + V_L)$), m^{-1}. A_S was effective mass transfer area, m^2. V_L was liquid phase volume including liquid slug and liquid film, m^3. $C_{CO_2}^{L}$ was CO_2 concentration in bulk liquid phase solution along the serpentine microchannel, mol/m^3. $C_{CO_2}^{*,L}$ was saturated solubility of CO_2 in aqueous MEA solution, mol/m^3, which was calculated based on Henry's Law,

$$C_{CO_2}^{*,L} = \frac{P_{CO_2}}{1000 H_{CO_2}^{loaded}} \tag{16}$$

where $H_{CO_2}^{loaded}$ is Henry's constant of CO_2 in the loaded aqueous MEA solution with CO_2, kPa·m^3·mol^{-1}, which can be estimated by N_2O approximation method,[37-41]

9

1

$$\frac{H_{CO_2}^{loaded}}{H_{N_2O}^{loaded}} = \frac{H_{CO_2}^{H_2O}}{H_{N_2O}^{H_2O}} \tag{17}$$

2

$$\ln\left(H_{N_2O}^{H_2O}\right) = -700.6501 + 14905.5017/T + 126.3505\ln T - 0.2267T \tag{18}$$

3   Henry's constant of CO_2 in water was proposed by Versteeg and van Swaaij,[42]

4

$$H_{CO_2}^{H_2O} = 2.8249\times10^3 \exp\left(-2044/T\right) \tag{19}$$

5   where $H_{CO_2}^{loaded}$ is Henry's constant of CO_2 and N_2O in the loaded aqueous MEA

6   solution with CO_2, kPa·m^3·mol^{-1}; $H_{CO_2}^{H_2O}$ and $H_{N_2O}^{H_2O}$ are Henry's constants of CO_2 and

7   N_2O in water, respectively, kPa·m^3·mol^{-1}. For the loaded aqueous MEA solution

8   system, the correlation of Henry's constant was proposed by Hartono et al..[41]

9

$$\ln\left(H_{N_2O}^{loaded}\right) = \ln\left(\Delta H_{N_2O}^{loaded}\right) + \ln\left(H_{N_2O}^{unloaded}\right) \tag{20}$$

10

$$\ln\left(\Delta H_{N_2O}^{loaded}\right) = 0.77m_{MEA} + 0.033m_{MEA}\alpha T \tag{21}$$

11

$$\ln\left(H_{N_2O}^{unloaded}\right) = \ln\left(\Delta H_{N_2O}^{unloaded}\right) + \varphi_{MEA}\ln\left(H_{N_2O}^{MEA}\right) + \varphi_{H_2O}\ln\left(H_{N_2O}^{H_2O}\right) \tag{22}$$

12

$$\ln\left(\Delta H_{N_2O}^{unloaded}\right) = \left(1.9210 - 1.6792\times10^{-3}T + 3.0951m_{MEA}^2\right)m_{MEA}\left(1-m_{MEA}\right)\sqrt{1-\varphi_{MEA}^2} \tag{23}$$

13

$$\varphi_{MEA} = \frac{m_{MEA}M_{MEA}/\rho_{MEA}}{m_{MEA}M_{MEA}/\rho_{MEA} + \left(1-m_{H_2O}\right)M_{H_2O}/\rho_{H_2O}} \tag{24}$$

14

$$\ln\left(H_{N_2O}^{MEA}\right) = 3.9451 - \frac{589.9365}{T - 99.0406} \tag{25}$$

15   where $\Delta H_{N_2O}^{loaded}$ and $\Delta H_{N_2O}^{unloaded}$ were the apparent Henry's constant deviation in

16   aqueous MEA solution with and without CO_2, kPa·m^3·mol^{-1}. $H_{N_2O}^{unloaded}$ was Henry's

17   constant of N_2O in aqueous MEA solution without CO_2, kPa·m^3·mol^{-1}. m_{MEA} and

18   m_{H_2O} were the mole fraction of MEA and H_2O in aqueous MEA solution, respectively.

19   α was CO_2 loading in aqueous MEA solution, mol_{CO_2}/mol_{MEA}. φ_{MEA} and φ_{H_2O} were

20   the volume fraction of MEA and H_2O, respectively. $H_{N_2O}^{MEA}$ was Henry's constant of

21   N_2O in MEA, kPa m^3 mol^{-1}. M_{MEA} and M_{H_2O} were the molecular mass of MEA and

10

1 H_2O, respectively, kg $\cdot$mol^{-1}. ρ_{MEA} and ρ_{H_2O} were the density of MEA and H_2O,

2 respectively, kg m^{-3}. The reaction between MEA and CO_2 was considered as a fast

3 irreversible process. In this case, CO_2 concentration in the bulk liquid phase was

4 assumed zero, given that the liquid side mass transfer coefficient was significantly

5 lower than the apparent reaction rate as analyzed by Kasturi and Stepanek.[43]

6 **3.3. Determination of Bubble Volume**

7 Figure 2(b) shows the bubble cross-section model. Its volume and surface area

8 were expressed by the following.[14,44]

9
$$V_{CO_2} = \left[(\pi - 4)I^2 + (d_H - 2\delta)^2 \right](L_B - d_H) + \frac{4}{3}\pi(0.5d_H - \delta)^3 \tag{26}$$

10
$$A_S = \left[2\pi I + 4(d_H - 2\delta - 2I) \right](L_B - d_H) + 4\pi(0.5d_H - \delta)^2 \tag{27}$$

11 where *I* was the radius of the quadrant at the corner and obtained from the captured

12 images, m. d_H and L_B were the hydraulic diameter and the length of Taylor bubble,

13 respectively, m. δ denoted the liquid film thickness near the channel wall center and

14 estimated by the correlation from Aussillous and Quéré[45]

15
$$\frac{\delta}{D_H} = \frac{0.67Ca^{2/3}}{1 + 3.35Ca^{2/3}} \tag{28}$$

16
$$Ca = \frac{\mu_L U_B}{\gamma_{TP}} \tag{29}$$

17 where *Ca* was capillary number. μ_L was the liquid phase viscosity, Pa s. γ_{TP} was the

18 gas-liquid two-phase interfacial tension and expressed by the correlation proposed by

19 Vázquez et al.[46]

20
$$\gamma_{TP} = \gamma_{H_2O} - \left(\gamma_{H_2O} - \gamma_{MEA} \right)\left(1 + \frac{0.6272m_{H_2O}}{1 - 0.9465m_{H_2O}} \right)m_{MEA} \tag{30}$$

11

1 where γ_{H_2O} and γ_{MEA} were the surface tension of pure water and MEA, respectively,

2 N/m (25°C, $\gamma_{H_2O} = 0.07201, \gamma_{MEA} = 0.04895$). The solution viscosity of the aqueous

3 MEA solution without CO_2 was calculated by the correlation by Hartono et al.[41]

$$\ln\left(\mu^{unloaded}\right) = m_{MEA}\left(8.36 - 4.664 \times 10^{-2}\,t + 1.6 \times 10^{-4}\,t^2 - 4.14 m_{MEA}\right)m_{H_2O}$$
$$+ m_{H_2O}\ln\left(\mu_{H_2O}\right) + m_{MEA}\ln\left(\mu_{MEA}\right) \tag{31}$$

5 where $\mu^{unloaded}$ was the viscosity of aqueous MEA solution without CO_2 absorption,

6 Pa s. μ_{MEA} and μ_{H_2O} were the viscosity of pure MEA and water, Pa s (25°C,

7 $\mu_{H_2O} = 8.937 \times 10^{-4}$; $\mu_{MEA} = 1.79 \times 10^{-2}$). t was the solution temperature, ^{o}C. The

8 concentration of MEA was very low, and the solution viscosity with CO_2 was replaced

9 by $\mu^{unloaded}$. So, the film thickness was calculated from Eqs. (28)-(31).

10 In this work, L_{CO_2} and U_B were calculated along the microchannel by 1000

11 continuously captured images. The bubble volume was calculated by Eq. (26) along

12 the channel position, and then dV_B/dX. The liquid phase volume within the unit cell

13 was determined from the formation frequency of the liquid slug. The gas phase

14 pressure was measured by the pressure sensor. The equilibrium solubility along the

15 channel position was calculated by Eqs. (16)-(25). Finally, E and k_La were calculated

16 by Eqs. (12) & (15), respectively.

4. RESULTS AND DISCUSSION

4.1. Length and Velocity of Gas Bubbles

19 The stable gas-liquid Taylor flow was formed at the T-junction and tracked along

20 the serpentine microchannel. Figure 3 illustrates the evolution of CO_2 bubbles with

21 and without chemical reaction along the microchannel. More experimental data are

12

1   shown in Figure S1 of Supporting Information (SI). As bubbles moved downstream,

2   their length gradually decreased and finally leveled off, indicating CO_2 absorption

3   reached equilibrium, which was similar to CO_2-H_2O system.[14]

4
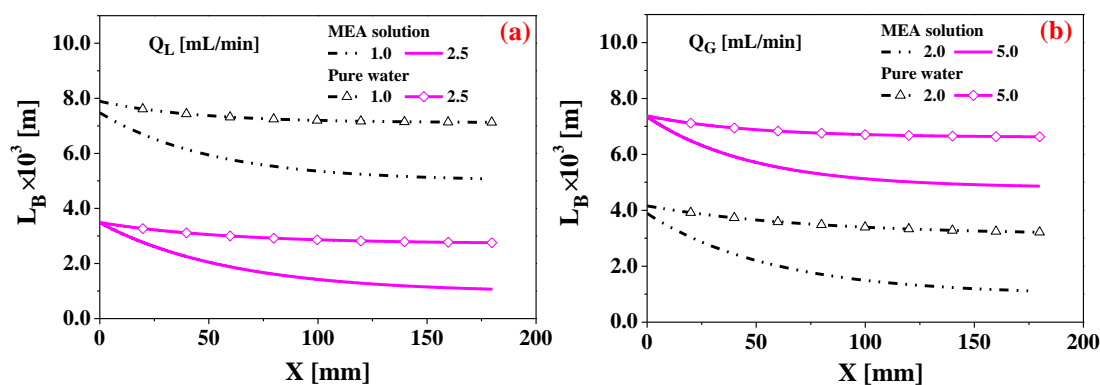
5   **Figure 3.** The evolution of Taylor bubble length along the serpentine microchannel at

6   25 °C, 1.0 atm and W_{MEA}=1 wt% for (a) Q_G = 5.5 mL/min, and (b) Q_L = 1 mL/min.

7   Initial bubble length at the T-junction (X=0) decreased with an increase in the

8   liquid flow rate (1.0-2.5 mL/min) (Figure 3(a) & Figure S1(a)), or with reducing gas

9   flow rates (Figure 3(b) & Figure S1(b)). Compared to CO_2-H_2O system, the initial

10   bubble length appeared reduced considerably, where the reducing extent decreased

11   with increasing liquid flow rate for a given gas flow rate. These phenomena were the

12   results of the combination of the physical properties of the solution and chemical

13   reaction. The increase in MEA content (0-1 wt%) in solution led to the increasing of

14   the liquid viscosity and the decreasing of gas-liquid interfacial tension, as shown in

15   Table 2. Because the variation of the interfacial tension was very small (72.01-71.18

16   N·m), the effects of the gas-liquid interfacial tension on the initial bubble length were

17   insignificant.[47] Previous studies have shown the initial bubble length decreased with

18   the increasing of the liquid phase viscosity.[10,48] In addition, the mass transfer with

19   chemical reaction during the formation of Taylor bubble further decreased the initial

13

1   bubble length.[49]

2   **Table 2.** Liquid phase viscosity and gas-liquid interfacial tension

W_{MEA}/wt%	0	1.0	1.5	2.0	2.5	3.0
$\mu \times 10^{-3}$/Pa s	0.894	0.921	0.936	0.950	0.965	0.980
$\gamma \times 10^{-3}$/N m	72.01	71.18	70.79	70.42	70.06	69.71

3   During Taylor bubble flowing along the microchannel, the shrinkage of CO_2 bubble

4   was accelerated by chemical reaction in comparison to CO_2-H_2O system (Figure 3 &

5   Figure S1). In the first 60 mm (X≤ 60 mm) section, which was named as the rapid

6   shrinkage stage, Taylor bubble shrank rapidly where approximate 70% of total length

7   reduction (ΔL_B) was observed. In the second 60 mm (60<X≤ 120 mm) section, the

8   reduction of ΔL_B approached 25%, which was regarded as the moderate shrinkage

9   stage. In the third 60 mm (120<X≤ 180 mm) section, the bubble length kept almost

10   constant where only 5% of ΔL_B was completed, suggesting an equilibrium shrinkage

11   stage. This originated from the interplay of three competitive factors during the

12   evolution of the bubbles, i.e., CO_2 dissolution, chemical reaction and gas-liquid

13   two-phase pressure drop.

14   As found in our previous work,[14] the evolution of the bubbles along the

15   microchannel was determined by CO_2 dissolution and pressure drop. The existence of

16   chemical reaction in the present work could intensify the shrinkage of Taylor bubble,

17   which led to shorter bubble lengths and 70% of ΔL_B at the rapid shrinkage stage, as

18   shown in Figure 4. With the bubble flowing downstream, MEA was gradually

19   consumed, the reaction rate was weakened, and the decrease in bubble length reduced
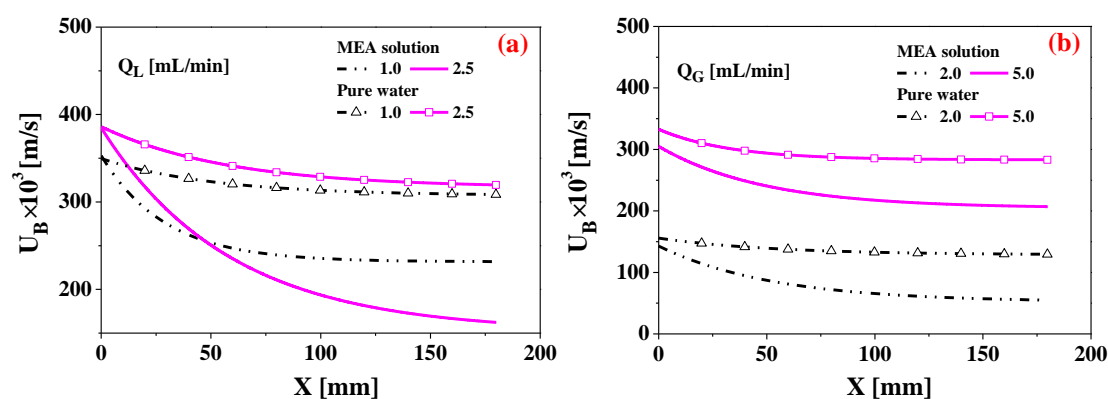
14

1   and finally leveled off.
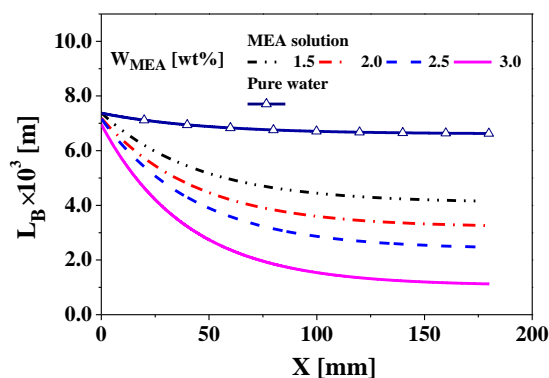
Figure 4. The effects of MEA content on the bubble length of along the serpentine microchannel for Q_G=5 mL/min and Q_L=1 mL/min.

Figure 5 & Figure S2 depict the evolution of Taylor bubble velocity accompanied with and without chemical reaction along the serpentine microchannel by varying gas (or liquid) flow rate. It was also observed that the bubble velocity decreased drastically for aqueous MEA solution, compared to the CO_2-H_2O system. The reduction in Taylor bubble velocity at three stages (the rapid, moderate and equilibrium shrinkage stages) were found to be 75%, 19% and 6% for a given gas flow rate, respectively. Figure 5(a) & Figure S2(a) also present the existence of a critical point during the evolution of the bubble velocity for CO_2-MEA system. It was attributed to the competition of two kinds of modes when increasing in liquid flow rate. One was the increase in the bubble velocity (the increasing mode), while the other one was the increase in the absorption rate that reduced the bubble velocity (the decreasing mode). As could be seen from Figure 5(a) & Figure S2(a), the bubble velocity increased with the liquid flow rate before the critical point, indicating that the increasing mode was dominant. After the critical point, the decreasing mode began to dominate. Figure 5(b) & Figure S2(b) shows Taylor bubble velocity increased with

15

increasing gas flow rate for a given liquid flow rate. Obviously, the gas flow rate

dominated over the increase in bubble velocity. The reductions in bubble velocity at

three stages were 72%, 22% and 6% for a given liquid flow rate, respectively. The

effects of MEA content on bubble velocity are shown in Figure 6. The reduction in

bubble velocity in three stages was found to be 83%, 14% and 3%, respectively. The

changes of in bubble velocity were similar to that of CO_2 bubble length as displayed

in Figure 4. The results allowed us to identify key parameters such as flow rate and

absorption rate for understanding and quantifying the dynamic evolution of

mass transfer.
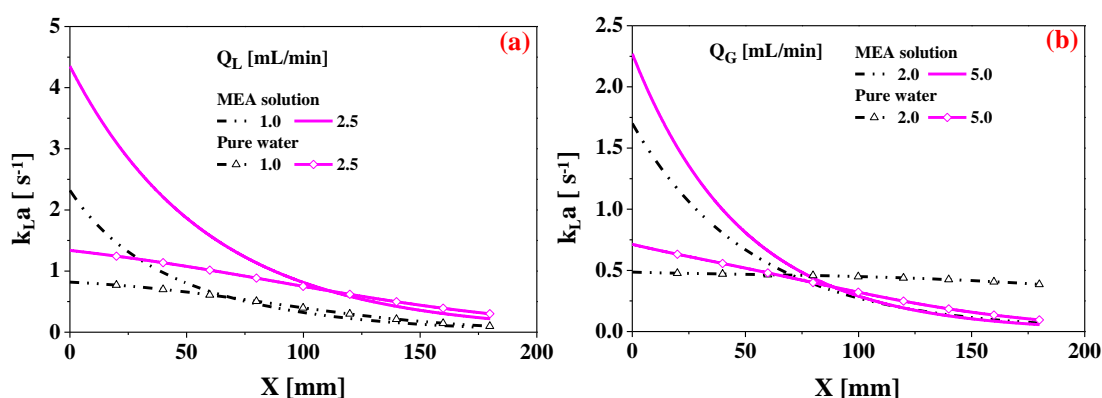

Figure 5. The evolution of Taylor bubble velocity along the serpentine microchannel

at 25 ^{o}C, 1.0 atm and W_{MEA}=1 wt% for (a) Q_G=5.5 mL/min, and (b) Q_L=1 mL/min.
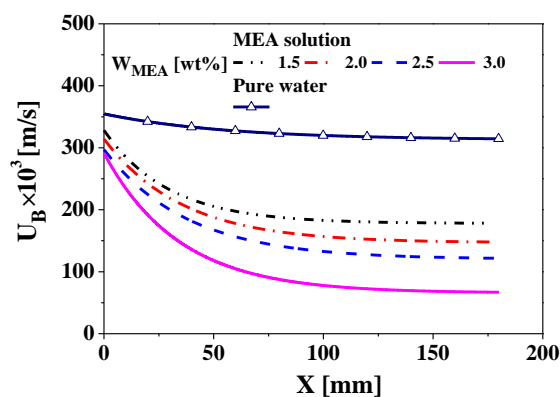
Figure 6. The effects of MEA content on the velocity of Taylor bubble along the

serpentine microchannel for Q_G=5 mL/min and Q_L=1 mL/min.

16

**4.2. Gas-Liquid Mass Transfer Coupled with Chemical Reaction**

$k_L a$, k_L and a are generally regarded as key parameters to characterize the gas-liquid mass transfer. Figure 7 & Figure S3 show the comparison of measured $k_L a$ along the serpentine microchannel for CO_2-H_2O and CO_2-MEA systems. Compared to CO_2-H_2O system, $k_L a$ increased considerably due to the chemical reaction. For a given gas (or liquid) flow rate, $k_L a$ increased with the increasing of liquid (or gas) flow rate. The effects of the liquid flow rate were more significant, which could be also attributed to the role of chemical reaction. Moreover, $k_L a$ in a unit cell decreased along the microchannel for both CO_2-H_2O and CO_2-MEA system, where the latter exhibited more dramatic decrease.

Figure 7. The effects of the gas or liquid flow rate on $k_L a$ in a unit cell along the serpentine microchannel at 25 ^{o}C, 1.0 atm and W_{MEA}=1 wt% for (a) Q_G= 5.5 mL/min, and (b) Q_L = 1 mL/min.

In the rapid shrinkage stage (X≤60 mm), approximate 78% reduction in $k_L a$ ($\Delta(k_L a)$) was obtained, where $\Delta(k_L a)$ denoted the difference between the initial (X=0 mm) and the end (X=180 mm) of the volumetric liquid phase mass transfer coefficient in a unit cell. In the moderate shrinkage stage (60<X≤120 mm), $\Delta(k_L a)$ approached 17%. In the equilibrium shrinkage stage (120<X≤180 mm), the value of $k_L a$ decreased until

17

1 becoming almost constant, where only 5% occurred. The effects of MEA content on

2 k_La are depicted in Figure 8. k_La increased with increasing MEA content due to the

3 reaction enhancement. About 78% and 17% reduction in k_La were obtained in the first

4 and second stages, respectively. The significantly higher reduction in the first stage

5 demonstrated the kinetic effect of the fast reaction.
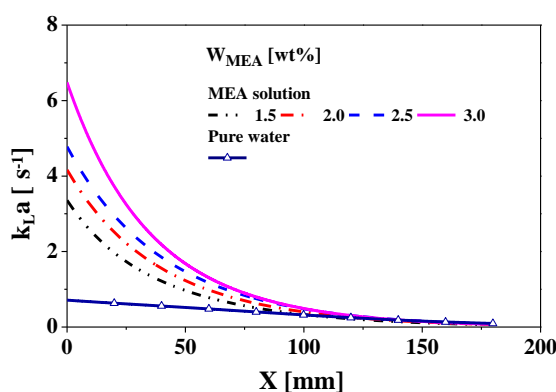
Figure 8. The effects of MEA content on k_La in a unit cell along the serpentine
microchannel at 25 ^{o}C and 1.0 atm for Q_G = 5 mL/min and Q_L = 1 mL/min.

9 In order to further elucidate the gas-liquid mass transfer performance for CO_2-MEA

10 system, k_L and a were separately analyzed. Figure 9 & Figure S4 compares the

11 evolution of k_L along the microchannel for both CO_2-MEA and CO_2-H_2O systems.

12 The decrease of k_L in CO_2-MEA system was more dramatic than that in CO_2-H_2O

13 system due to the intensification of chemical reaction, which was found to be 68%, 24%

14 and 8% in three stages, respectively.

15 For a given gas flow rate, k_L increased with the increasing liquid phase flow rate,

16 but decreased sharply as Taylor bubbles moved downstream along the microchannel

17 for CO_2-MEA system (Figure 9(a) & Figure S4(a)), which was determined

18 synergistically by the leakage flow in the liquid film and the circulation in the liquid

19 slug. Taylor bubble velocity decreased sharply for CO_2-MEA system (Figure 5(a) &

18

1   Figure S2(a)), which led to the significant decrease of the circulation and then k_L, and

2   such effects were weakened gradually along the microchannel. In addition, increasing

3   the viscosity of aqueous MEA solution (Table 2) could also decrease k_L by reducing

4   the diffusion coefficient and the circulation. However, the substantial decrease of the

5   bubble length (Figure 3(a) & Figure S1(a)) caused the reduction of the liquid film

6   length between the bubble and the channel wall, where the leakage flow in the film

7   was enhanced and in favor of increasing k_L. With the consumption of MEA in liquid

8   phase, the effect of chemical reaction was gradually weakened, where k_L approached

9   to CO_2-H_2O system. Finally, both positive and negative effects on k_L determined the

10   results of Figure 9(a) & Figure S4(a).

11
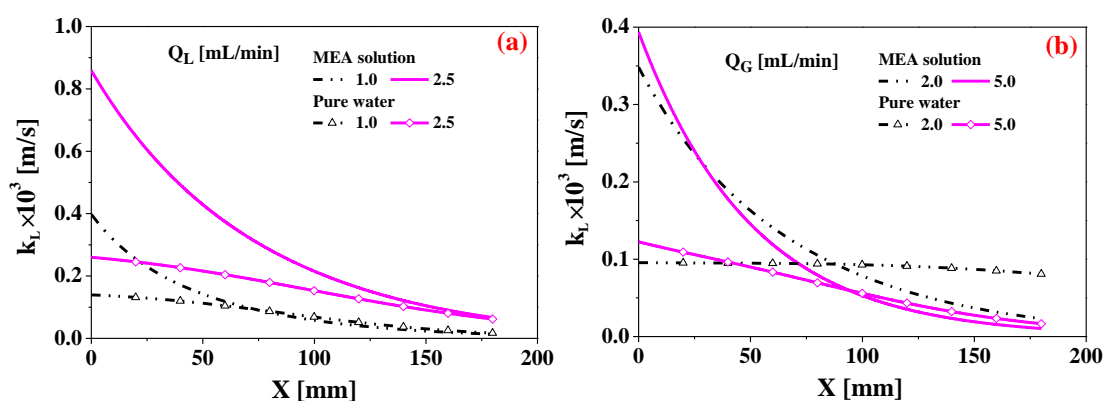
Figure 9. The evolution of k_L in a unit cell along the serpentine microchannel at 25 ^{o}C,

   1.0 atm and W_{MEA}=1 wt% for (a) Q_G = 5.5 mL/min, and (b) Q_L = 1 mL/min.

14   For a given liquid flow rate, there was also a critical position (X ≈ 25mm) for k_L

15   along the microchannel (Figure 9(b) & Figure S4(b)), where the reductions in k_L at

16   three stages were 67%, 24% and 9%, respectively. When X < 25 mm, k_L increased

17   with the increase in the gas phase flow rate, and decreased as X > 25 mm. This was

18   similar to the conclusion of our previous work.[14] However, the point moved forward

19   compared to CO_2-H_2O system. As we all known, CO_2 absorption capacity was

19

1   constant for a given initial MEA content, the larger the bubble length or the gas flow

2   rate was, the more decreasing extent of free MEA molecule and CO_2 absorption,

3   which weakened dramatically the intensification of chemical reaction on k_L as

4   absorption proceeded. Simultaneously, the liquid slug velocity decreased due to CO_2

5   absorption, which also reduced the circulation in the liquid slug. On the other hand,

6   the increasing gas flow rate and the decreasing bubble length were in favor of k_L by

7   enhancing the circulation and the leakage flow, respectively. Compared to CO_2-H_2O

8   system, both the negative and positive effects on k_L were enlarged due to chemical

9   reaction, and finally the critical point occurred in advance for CO_2-MEA system.

10
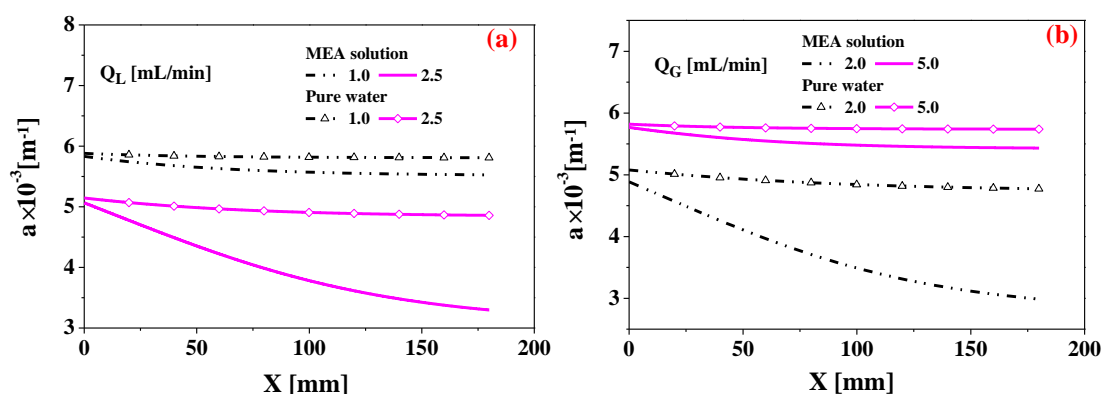
11   **Figure 10.** The evolution of a in a unit cell along the serpentine microchannel at 25

12    $^{\circ}$C, 1.0 atm and W_{MEA}=1 wt% for (a) Q_G = 5.5 mL/min, and (b) Q_L = 1 mL/min.

13   Figure 10 & Figure S5 shows the evolution of a in a unit cell along the serpentine

14   microchannel. The reduction of a in three stages were 57%, 30% and 13%,

15   respectively, which were smaller than the variation of k_L. Compared to CO_2-H_2O

16   system under the identical conditions, the decrease of a was accelerated as Taylor

17   bubbles moved downstream along the microchannel, especially for the initial shorter

18   bubble length which approached to spherical (i.e., bubble sphericity Φ), as shown in

19   Figure 11 & Figure S6. The effects of MEA content on gas-liquid mass transfer

20

1   performance, in terms of k_L, a and Φ, are depicted in Figure 12. The reductions in a

2   and k_L in three stages were 60%, 30% and 10%, respectively. It was observed k_L and

3   its reducing degree increased with increasing MEA content. On the one hand, the

4   decrease in the length of the bubble and the liquid film could lead to the increase of k_L.

5   On the other hand, both the decrease of the bubble velocity and the increase of the

6   liquid phase viscosity resulted in the decrease of k_L by weakening the circulation.

7   Finally, the positive and negative factors from MEA content together determined the

8   dynamic changes of k_L (Figure 12(a)). As generally known, the increase of MEA

9   content resulted in increasing CO_2 absorption rate and capacity in aqueous MEA

10   solution, which further accelerated the decrease of bubble length and the increase of

11   its Φ, and led to the decrease of a (Figure 12(b) & (c)).
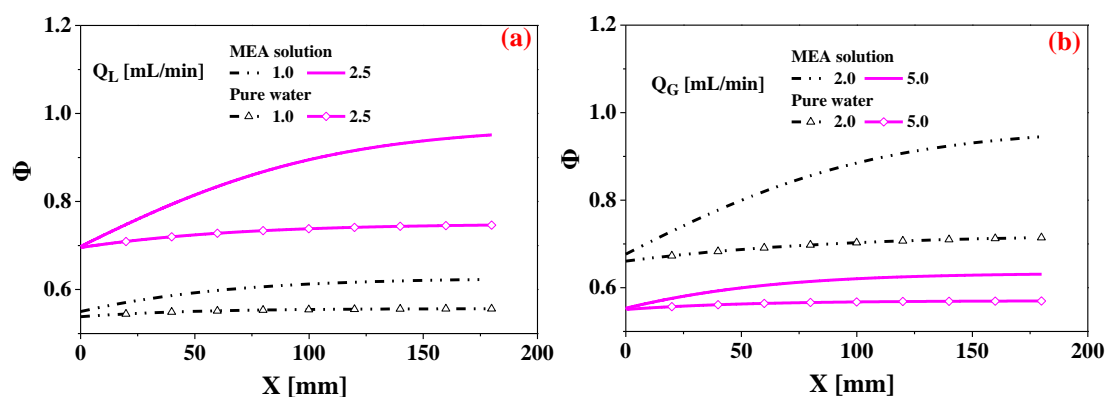
13   **Figure 11.** The evolution of the sphericity (Φ) along the serpentine microchannel, at

14   25 °C, 1.0 atm and $W_{MEA}=1$ wt% for (a) $Q_G = 5.5$ mL/min, and (b) $Q_L = 1$ mL/min.

21

1
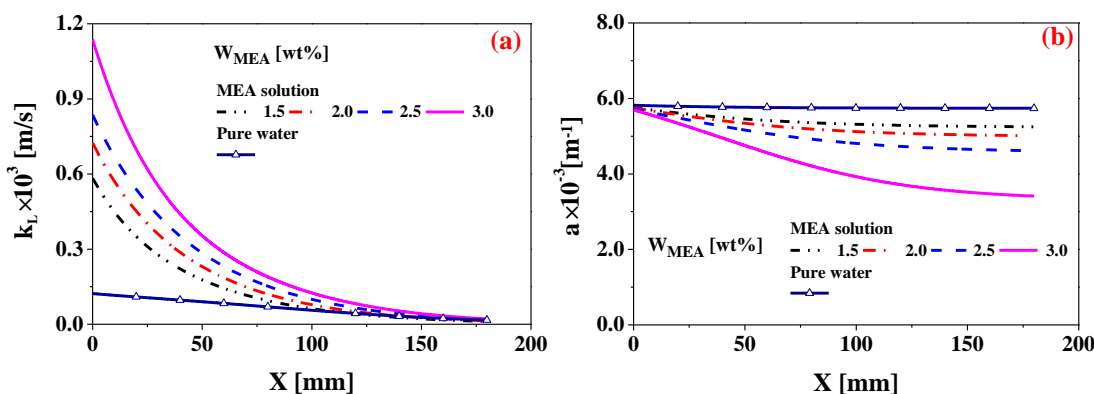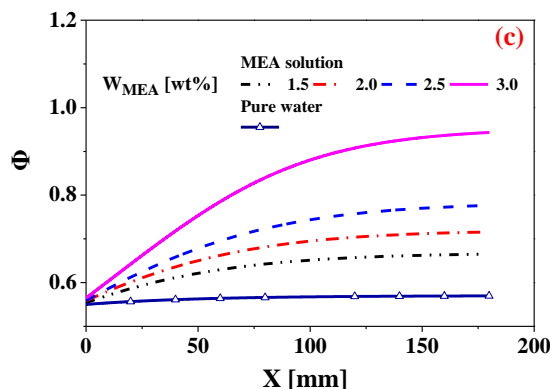
2   **Figure 12.** The effects of the MEA content on a (a), k_L (b) and Φ (c) along the

3   serpentine microchannel at 25 ^{o}C, 1.0 atm for Q_G = 5 mL/min and Q_L = 1 mL/min.

4   **4.3. Dynamic Changes of the Enhancement Factor**

5   It was reasonably expected that gas-liquid two-phase mass transfer performance

6   could be enhanced by chemical reaction for CO_2-MEA system. To quantitatively

7   characterize the process, E was adopted to represent the ratio of mass transfer between

8   with and without chemical reaction. However, the local dynamic conditions are

9   generally difficult to measure directly in any reactor because the mass transfer never

10   stops before reaching the absorption equilibrium, representing the dynamic process of

11   gas-liquid two-phase flow. Figure 13(a) demonstrates the dynamic changes of E_{exp}

12   along the microchannel at four MEA contents, where the experimental enhancement factor

13   (E_{exp}) of CO_2-MEA system was calculated from the following equation by taking into account of

14   both k_L^0 and k_L.

$$E_{exp} = \frac{k_L \left(C_{Ai} - C_{CO_2}^L \right)}{k_L^0 C_{CO_2}^{*,L}} \tag{32}$$

16   where k_L^0 denotes the physical mass transfer coefficient for identical operating

17   conditions at the entrance of microchannel for CO_2-H_2O and CO_2-MEA system. That

18   is, the maximum physical mass transfer coefficient is chosen for a given operating

22

1   condition.

2   For a given gas and liquid flow rate, E increased with the increasing MEA content

3   and also decreased gradually as Taylor bubbles moved downstream along the

4   microchannel. The chemical reaction rate was proportional to MEA content.

5   Furthermore, the viscosity of the solution increased with the increase of MEA content,

6   which could weaken the influence of chemical reaction. As Taylor bubbles moved

7   beyond the critical value, E tended to be stable and close to one, indicating that the

8   intensification of the chemical reaction was weakened until to be ignored. This

9   suggested the microchannel length could be optimized based on the above critical

10   position for the design of gas-liquid two-phase low pressure drop microchannel

11   reactor.

12   The enhancement factor (E_{exp}) of CO_2-MEA system agreed well with the calculated

13   enhancement factor (E_{cal}) from Eq. 12, which indicated the validity of the model, as

14   shown in Figure 13(b). Hikita et al.[50] investigated the kinetics of the reaction of CO_2

15   with MEA for MEA concentration in the range of 0.0152-0.177 mol/L at temperatures

16   ranging from 5.6 $^{\circ}$C to 35.4 $^{\circ}$C, and found the reaction to be an irreversible second

17   order reaction. In the present work, the initial MEA concentration was varied in the

18   range of 0.163-0.490 mol/L, so the reaction rate can be expressed reasonably by the

19   second-order model. Furthermore, Santiago and Farina[51] demonstrated that the

20   accuracy of the prediction of this model was 3% for fast second order and irreversible

21   reactions with Ha > 3. In the present work, Ha values (Figure 13(c)) fit well in the

22   range stated by Santiago and Farina, further supporting suitability of the expression
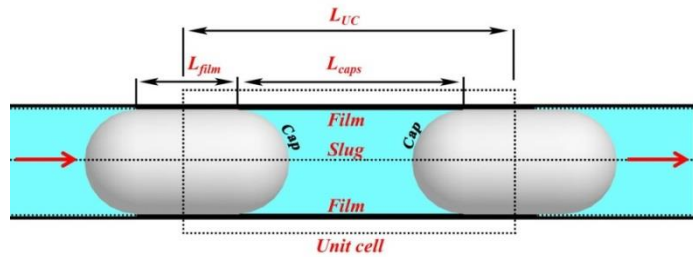
23

1   used in the study.

2

3
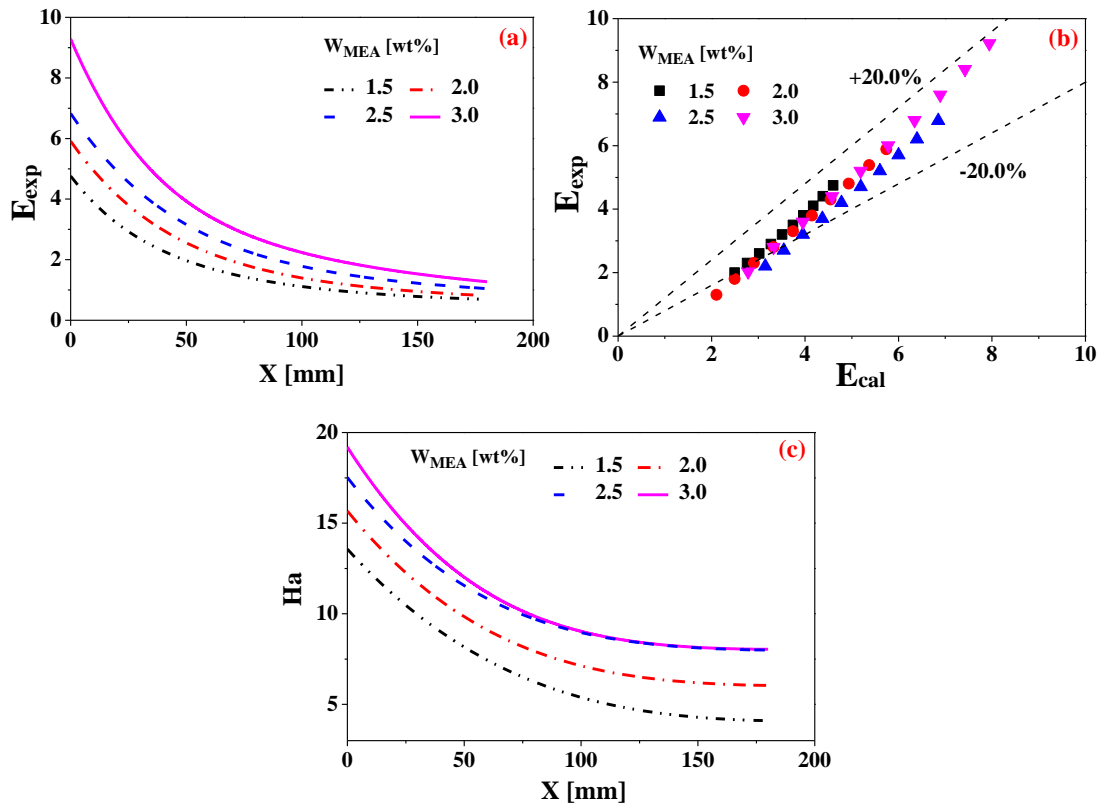
4   **Figure 13.** The effects of MEA content on E in a unit cell along the serpentine

5   microchannel (a), prediction of E (b) and Ha (c) for CO_2-MEA system at 25 $^{\circ}$C, 1.0

6   atm $Q_G = 5$ mL/min and $Q_L = 1$ mL/min.

7   **4.4. Empirical Correlations for Mass Transfer Performance**

8

9   **Figure 14.** Schematic overview of unit cell, bubble, slug and film.

10   In order to further investigate and predict the mass transfer of the unit cells

11   detailedly, the improved mass transfer model proposed by van Baten and Krishna,[16]

12   was introduced to verify experimental data. The core principle of the model was that

24

1   the contributions from caps $(k_L a)_{caps}$ and film $(k_L a)_f$ to mass transfer were evaluated

2   based on Higbie's penetration theory. The improved mass transfer model was shown

3   in the following.

4
$$k_L a = \frac{2\sqrt{2}}{\pi}\sqrt{\frac{D_{CO_2} U_{B\text{-}sat}}{d_H}}\frac{4}{L_{UC}} + \frac{2}{\sqrt{\pi}}\sqrt{\frac{D_{CO_2} U_{B\text{-}sat}}{\varepsilon_V L_{UC}}}\frac{4\varepsilon_V}{d_H} \tag{33}$$

5   where $U_{B\text{-}sat}$, ε_V and L_{UC} were the difference of the transient bubble velocity and the

6   saturated bubble velocity for absorption equilibrium state, the gas void fraction based

7   on the unit cell volume and the unit cell length, respectively.

8   It was well known that the basic assumption of van Baten's model (Eq. (33)) was

9   the ideal mixing in the liquid slug for a unit cell. Actually, there was a big

10   concentration distribution in the liquid slug,[52] so van Baten's model was difficult to

11   accurately predict the experimental data of this work. Considering that the deviation

12   mainly originated from the non-ideal mixing in the liquid slug by mass exchange with

13   the liquid film layer close to the wall, a correction term in the form of Eq. (34) was

14   proposed.

15
$$(k_L a)_C = \frac{3.66 D_{CO_2}}{d_H}\frac{L_S (d_H - 2\delta)}{d_H^2 L_{UC}} \tag{34}$$

16   This mass exchange between the slug and liquid film layer could be approximated

17   under-developed laminar flow in a circular channel with a constant boundary,[53,54] as

18   well as considering the ratio of the slug length to the unit cell length. The above

19   correlation was derived from the classical theory, where the caps were assumed

20   perfectly spherical and the film was annular due to the circular capillary in van

21   Baten's model. Compared to the non-spherical caps and the non-annular film due to

1   the square microchannel in this work, it was necessary to modify the parameters in

2   order to fit the experimental data, as shown in Table 3.

3   As shown in Eq. (34), $(k_L)_C$ is set as $3.66 D_{CO2}/d_H$ since the film-slug exchange is

4   initially simplified as flowing in a circular channel with fully developed laminar flow.

5   Thus, underdeveloped laminar flow in the liquid film and different thickness of the

6   liquid film in the cross section require the modification of ideal $(k_L)_C$. In this case, the

7   additional constant is added to the semi-empirical correlation according to the

8   experimental data.

9   The validity of the models for both CO_2-H_2O and CO_2-MEA systems are shown in

10   Figures 15 & 16, respectively. The predicted values were well aggreement with the

11   experimental results for a deviation of ± 25%. Applying the model for CO_2-H_2O

12   system to CO_2-MEA system, the net physical mass transfer coefficient could be

13   approximately separated from chemical absorption process.

14   The basic assumption of van Baten's model was the ideal mixing in the liquid slug

15   for a unit cell without concentration gradient, where the overall mass transfer

16   coefficient of the unit cell could be considered as the sum of the overall mass transfer

17   coefficients from two caps and the film, $k_L a = (k_L a)_{caps} + (k_L a)_f$. This was inconsistent

18   with the situation where concentration difference existed between the film and the

19   bulk liquid slug, and the mass exchange was mainly determined by the internal

20   circulation in the bulk liquid slug. This is believed to be the main reason for the

21   inconsistence shown in Figures 15 and 16 for fitting the correlations (Table 3) with

22   the measured data. More experimental data are shown in Figure S7 & S8 of SI.

26

1

Table 3. Separated contributions for predicting k_La

System	$(k_La)_{caps}$ (1/s)	$(k_La)_{film}$ (1/s)	$(k_La)_C$ (1/s)	R^2
H_2O-CO_2	$\dfrac{1.4\sqrt{2}}{\pi}\sqrt{\dfrac{D_{CO_2} U_{B\text{-sat}}}{d_H}}\dfrac{4}{L_{UC}}$	$\dfrac{5.4}{\sqrt{\pi}}\sqrt{\dfrac{D_{CO_2} U_{B\text{-sat}}}{\varepsilon_v L_{UC}}}\dfrac{4\varepsilon_v}{d_H}$	$-13\dfrac{3.66 D_{CO_2}}{d_H}\dfrac{L_S(d_H\text{-}2\delta)}{d_H^2 L_{UC}}$	0.95
MEA-CO_2	$\dfrac{\sqrt{2}}{\pi}\sqrt{\dfrac{D_{CO_2} U_{B\text{-sat}}}{d_H}}\dfrac{4}{L_{UC}}$	$\dfrac{7.4}{\sqrt{\pi}}\sqrt{\dfrac{D_{CO_2} U_{B\text{-sat}}}{\varepsilon_v L_{UC}}}\dfrac{4\varepsilon_v}{d_H}$	$-35\dfrac{3.66 D_{CO_2}}{d_H}\dfrac{L_S(d_H\text{-}2\delta)}{d_H^2 L_{UC}}$	0.96

2

3
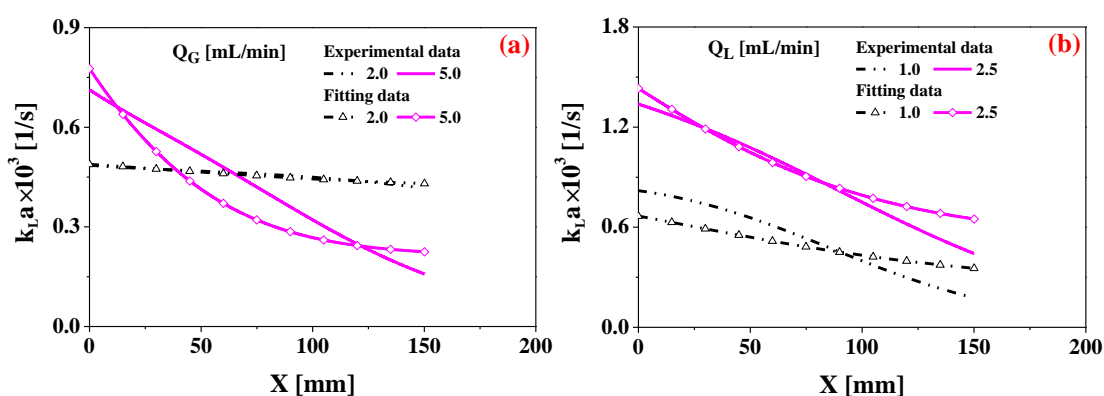
Figure 15. Prediction of overall mass transfer coefficients for CO_2-H_2O system at 25

^{o}C, 1.0 atm for (a) Q_L = 1 mL/min, and (b) Q_G = 5.5 mL/min.

6
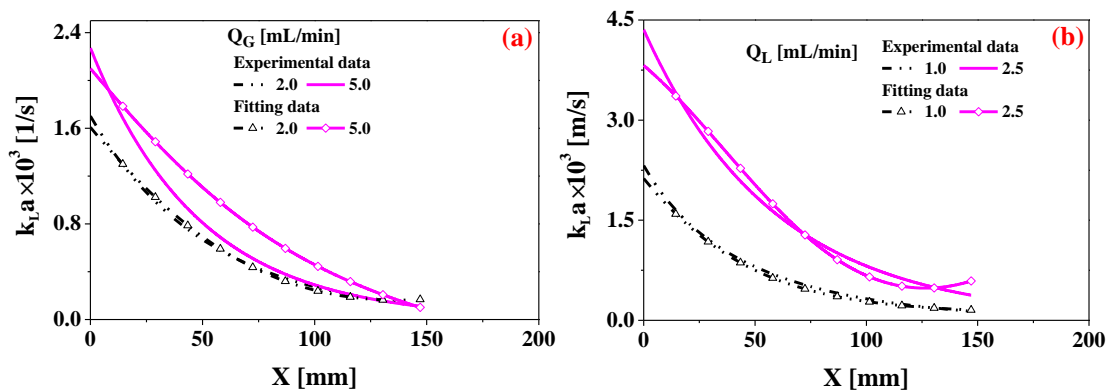
Figure 16. Prediction of overall mass transfer coefficients for CO_2-MEA system at 25

^{o}C, 1.0 atm and W_{MEA}=1 wt% for (a) Q_L = 1 mL/min, and (b) Q_G = 5.5 mL/min.

As analyzed above, the semi-empirical correlations were proposed to predict the

physical/chemical mass transfer coefficients in the CO_2-H_2O system. If the range of

the parameters in the empirical correlation is reasonably wide to adapt the situation of

27

1 chemical mass transfer coefficient, the enhancement factor can be estimated. It should

2 be noted that the semi-empirical correlations may not be suitable when beyond the

3 scope of the experimental conditions. For the CO_2-MEA system, the semi-empirical

4 correlation indeed reflects the effect of only an overall mass transfer coefficient

5 covering both mass transfer and chemical reactions. This is mainly due to the fact that

6 they are impractically measureable separately in the dynamic physical/chemical

7 coupling process, although approximate solutions may be obtained through numerical

8 analysis. The development in this work with in-situ measurements along

9 microchannels provides a practical approach to quantify the parameters in order to

10 estimate the overall apparent mass transfer coefficient in the CO_2-MEA system, which

11 is still difficult in the macroscale system. It can also be considered as a benchmark for

12 estimating the enhancement factor of other physical/chemical coupling systems

13 having different kinetics, such as CO_2-DEA and CO_2-MDEA. Nevertheless, by

14 incorporating a wider variety of experimental data a simpler empirical correlation

15 may be established for determining the enhancement factor. This is under active

16 investigation in our laboratories.

5. CONCLUSIONS

18 Dynamic coupling of mass transfer and chemical reaction during Taylor flow in

19 serpentine microchannels was experimentally characterized by an online method. The

20 dynamic changes of gas bubbles, and key mass transfer parameters including k_La, k_L

21 and a were measured or calculated under the optimized experimental conditions (i.e.,

22 Q_G, Q_L, W_{MEA}), respectively. The dynamic enhancement of mass transfer by chemical

28

1   reaction was further quantified in terms of E. Based on the experimental results, a

2   modified van Baten's model was proposed to predict mass transfer performance for

3   both CO_2-H_2O and CO_2-MEA systems and the R^2 values were 0.95 and 0.96,

4   respectively.

5   Overall, the dynamic shrinkage of Taylor bubbles flowing along the microchannel

6   was observed, showing more significant changes in CO_2-MEA system. Three stages

7   of the shrinkage of Taylor bubbles were observed, where about 70% of the length

8   reduction took place in the first stage, and lower change rates in other stages,

9   indicating the dynamic impact of the fast chemical reaction. Compared to CO_2-H_2O

10   system, $k_L a$ was considerably intensified due to chemical reaction for CO_2-MEA

11   system. The dynamic decrease and experiencing three stages of $k_L a$ in a unit cell was

12   also found along the microchannel for CO_2-MEA system, where $k_L a$ in the first stage

13   reached approximately 70%. k_L also decreased sharply as Taylor bubbles moved

14   downstream along the microchannel for CO_2-MEA system. For a given liquid flow

15   rate, the decreasing curves of k_L along the microchannel for different gas flow rates

16   crossed at a critical position, indicating the interplay between the effects of chemical

17   reactions and the physical shape of bubbles.

18   Finally, the dimensionless correlations on the mass transfer performance for both

19   CO_2-H_2O and CO_2-MEA systems showed that the calculated values agreed well with

20   the experimental results and the experimental results for a deviation of $\pm 25\%$,

21   demonstrating the feasibility of the model for predicting key mass transfer parameters.

22   The correlations also suggested the net physical mass transfer performance in

1   CO_2-MEA system could be reasonably separated from the chemical absorption

2   process.

6. SUPPORTING INFORMATION

4   Experimental data under other operating conditions, the derivation process of Eq. 5,

5   Eq.15 and Eq. 34 are shown in Supporting Information.

7. ACKNOWLEDGMENTS

NOMENCLATURE

a	=	specific surface area (m^{-1})
A_s	=	gas bubble surface area in a unit cell (m^2)
C_{CO_2}	=	CO_2 concentration in liquid phase ($mol \cdot m^{-3}$)
$C_{CO_2}^{*,L}$	=	saturated solubility of CO_2 in liquid phase ($mol \cdot m^{-3}$)
$C_{CO_2}^{L}$	=	CO_2 concentration in liquid phase ($mol \cdot m^{-3}$)
$C_{CO_2,i}$	=	CO_2 concentration at gas-liquid interface ($mol \cdot m^{-3}$)
C_{MEA}	=	MEA concentration in liquid phase ($mol \cdot m^{-3}$)
$C_{MEA,L}$	=	MEA concentration in the bulk liquid phase ($mol \cdot m^{-3}$)
$C_{MEA,0}$	=	initial MEA concentration in liquid phase ($mol \cdot m^{-3}$)
d_H	=	microchannel hydraulic diameter (m)
D_{CO_2}	=	diffusion coeffcient of CO_2 in aqueous MEA solution ($m^2 \cdot s^{-1}$)
D_{MEA}	=	diffusion coeffcient of MEA in aqueous MEA solution ($m^2 \cdot s^{-1}$)

30

E = enhancement factor

E_∞ = infinite enhancement factor

$H_{CO_2}^{loaded}$ = Henry's constant of CO_2 in the loaded liquid phase ($kPa \cdot m^3 \cdot mol^{-1}$)

$H_{N_2O}^{loaded}$ = Henry's constant of N_2O in the loaded liquid phase ($kPa \cdot m^3 \cdot mol^{-1}$)

$H_{CO_2}^{H_2O}$ = Henry's constant of CO_2 in water ($kPa \cdot m^3 \cdot mol^{-1}$)

$H_{N_2O}^{H_2O}$ = N_2O Henry's constant in water ($kPa \cdot m^3 \cdot mol^{-1}$)

$H_{N_2O}^{MEA}$ = N_2O Henry's constant in MEA ($kPa \cdot m^3 \cdot mol^{-1}$)

$\Delta H_{N_2O}^{unloaded}$ = Henry's constant deviation of N_2O in unloaded liquid ($kPa \cdot m^3 \cdot mol^{-1}$)

$\Delta H_{N_2O}^{loaded}$ = Henry's constant deviation of N_2O in loaded liquid ($kPa \cdot m^3 \cdot mol^{-1}$)

I = radius of the quadrant at the corner (m)

k_1 = second-order reaction rate constant ($m^3 \cdot mol^{-1} \cdot s^{-1}$)

k_L = liquid side mass transfer coefficient ($m \cdot s^{-1}$)

k_L^0 = liquid side physical mass transfer coefficient ($m \cdot s^{-1}$)

L_B = Taylor bubble length (m)

L_{caps} = length of liquid slug and two caps (m)

L_{film} = liquid film length (m)

L_S = liquid slug length (m)

L_{UC} = unit cell length (m)

m_{MEA} = mole fraction of MEA in aqueous MEA solution (mol%)

m_{H_2O} = mole fraction of MEA in aqueous MEA solution (mol%)

M_{MEA} = molecular mass of MEA ($kg \cdot mol^{-1}$)

M_{H_2O} = molecular mass of H_2O ($kg \cdot mol^{-1}$)

P_{CO_2} = gas phase pressure (Pa)

r_{CO_2} = CO_2 absorption rate in aqueous MEA solution ($mol \cdot m^{-3} \cdot s^{-1}$)

R = gas constant (8.3145 J/(mol·K))

t = solution temperature (^{o}C)

T = operating temperature (K)

U_B = gas bubble velocity ($m \cdot s^{-1}$)

U_{B-sat} = the difference between the transient bubble velocity and the saturated bubble velocity for absorption equilibrium state ($m \cdot s^{-1}$)

31

V_B	=	gas phase volume in a unit cell (m^3)
V_L	=	liquid phase volume in a unit cell (m^3)
W	=	microchannel width (m)
X	=	position of the serpentine channel (m)

Greek Symbols

α	=	loading of CO_2 (mol_{CO_2}/mol_{MEA})
γ_{H_2O}	=	surface tension of pure water ($N \cdot m^{-1}$)
γ_{MEA}	=	surface tension of pure MEA ($N \cdot m^{-1}$)
γ_{TP}	=	gas-liquid interfacial tension ($N \cdot m^{-1}$)
δ	=	liquid film thickness near the channel wall center (m)
ε_V	=	gas void fraction based on the unit cell volume
μ_L	=	aqueous MEA solution viscosity (Pa s)
$\mu^{unloaded}$	=	aqueous MEA solution viscosity without CO_2 (Pa s)
μ_{MEA}	=	viscosity of MEA (Pa s)
μ_{H_2O}	=	viscosity of water (Pa s)
ρ_{H_2O}	=	density of H_2O ($kg \cdot m^{-3}$)
ρ_L	=	density of aqueous MEA solution ($kg \cdot m^{-3}$)
ρ_{MEA}	=	density of MEA ($kg \cdot m^{-3}$)
φ_{H_2O}	=	volume fraction of H_2O
φ_{MEA}	=	volume fraction of MEA
Φ	=	bubble sphericity (the ratio of the surface area of a sphere to the surface area of a gas bubble with the same volume)

Dimensionless Parameters

Ca	=	capillary number ($Ca = (\mu_L U_B)/\gamma_L$)
Ha	=	Hatta number ($Ha = \sqrt{D_{CO_2} k_1 C_{MEA,L}}/k_L^0$)

32

REFERENCES

(1)   Mandal, B. P.; Biswas, A. K.; Bandyopadhyay, S. S. Absorption of carbon dioxide into aqueous blends of 2-amino-2-methyl-1-propanol and diethanolamine. *Chem. Eng. Sci.* **2003,** *58*(18)*,* 4137−4144.

(2)   Maceiras, R.; Álvarez, E.; Cancela, M. Á. Effect of temperature on carbon dioxide absorption in monoethanolamine solutions. *Chem. Eng. J.* **2008,** *138*(1−3)*,* 295−300.

(3)   Kashid, M. N.; Renken, A.; Kiwi-Minsker, L., Gas-liquid and liquid-liquid mass transfer in microstructured reactors. *Chem. Eng. Sci.* **2011,** *66*(17), 3876−3897.

(4)   Ye, C. B.; Chen, G. W.; Yuan, Q. Process characteristics of CO_2 absorption by aqueous monoethanolamine in a microchannel reactor. *Chin. J. Chem. Eng.* **2012,** *20*(1)*,* 111−119.

(5)   Metz, B.; Davidson, O.; Coninck, H. D.; Loos, M.; Meyer, L. Carbon Dioxide Capture and Storage; Cambridge Univ Press, UK, **2005**.

(6)   Luo, X.; Hartono. A.; Hussain, S.; Svendsen, H. F. Mass transfer and kinetics of carbon dioxide absorption into loaded aqueous monoethanolamine solutions. *Chem. Eng. Sci.* **2015,** *123,* 57−69.

(7)   Kobayashi, J.; Mori, Y.; Okamoto, K.; Akiyama, R.; Ueno, M.; Kitamori, T.; Kobayashi, S. A microfluidic device for conducting gas-liquid-solid hydrogenation reactions. *Science* **2004,** *304*(5675)*,* 1305−1308.

(8)   Fu, T. T.; Ma, Y. G.; Funfschilling, D.; Li, H. Z. Bubble formation and breakup mechanism in a microfluidic flow-focusing device. *Chem. Eng. Sci.* **2009,** *64*(10)*,* 2392−2400.

(9)   Sobieszuk, P.; Pohorecki, R.; Cyganski, P.; Grzelka, J. Determination of the interfacial area and mass transfer coefficients in the Taylor gas-liquid flow in a microchannel. *Chem. Eng. Sci.* **2011,** *66*(23)*,* 6048−6056.

(10) Yang, L.; Tan, J.; Wang, K.; Luo, G. S. Mass transfer characteristics of bubbly flow in microchannels. *Chem. Eng. Sci.* **2014,** *109*(16)*,* 306−314.

(11) Li, L.; Yao, C. Q.; Jiao, F. J.; Han, M.; Chen, G. W. Experimental and kinetic study of the nitration of 2-ethylhexanol in capillary microreactors. *Chem. Eng. Process.* **2017,** *117,* 179−185.

(12) Abiev, R. Sh.; Svetlov, S.; Hasse, S. Hydrodynamics and mass transfer of gas-liquid and liquid-liquid Taylor flow in microchannels. *Chem. Eng. Technol.* **2017,** *40*(11)*,* 1985−1998.

(13) Yao, C. Q.; Zhao, Y. C.; Chen, G. W. Multiphase processes with ionic liquids in microreactors: hydrodynamics, mass transfer and applications. *Chem. Eng. Sci.* **2018,** *189,* 340−359.

(14) Zhang, P.; Yao, C. Q.; Ma, H. Y.; Jin, N.; Zhang, X. L.; Lv, H. Y.; Zhao, Y. C. Dynamic changes in gas-liquid mass transfer during Taylor flow in long serpentine square microchannels. *Chem. Eng. Sci.* **2018,** *182,* 17−27.

(15) Berčič, G.; Pintar, A. The role of gas bubbles and liquid slug lengths on mass transport in the Taylor flow through capillaries. *Chem. Eng. Sci.* **1997**, *52*(21-22), 3709−3719.

(16) van Baten, J. M. V.; Krishna, R. CFD simulations of mass transfer from Taylor bubbles rising in circular capillaries. *Chem. Eng. Sci.* **2004**, *59*(12), 2535−2545.

(17) Yue, J.; Chen, G. W.; Yuan, Q.; Luo, L. A.; Gonthier, Y. Hydrodynamics and mass transfer characteristics in gas-liquid flow through a rectangular microchannel. *Chem. Eng. Sci.* **2007,** *62*(7)*,* 2096−2108.

(18) Yue, J.; Luo, L. A.; Gonthier, Y.; Chen, G. W.; Yuan, Q. An experimental study of air-water

Taylor flow and mass transfer inside square microchannels. *Chem. Eng. Sci.* **2009,** *64,* 3697−3708.

(19) Li, C. F.; Zhu, C. Y.; Ma, Y. G.; Liu, D. Z.; Gao, X. Q. Experimental study on volumetric mass transfer coefficient of CO2 absorption into MEA aqueous solution in a rectangular microchannel reactor. *Int. J. Heat Mass Transf.* **2014,** *78,* 1055−1059.

(20) Chu, C. Y.; Zhang, F. B.; Zhu, C. Y.; Fu, T. T.; Ma, Y. G. Mass transfer characteristics of CO_2 absorption into 1-butyl-3-methylimidazolium tetrafluoroborate aqueous solution in microchannel. *Int. J. Heat. Mass. Transfer.* **2019**, *128*, 1064–1071.

(21) Cubaud, T.; Sauzade, M.; Sun, R. P. CO_2 dissolution in water using long serpentine microchannels. *Biomicrofluidics* **2012,** *6*(2)*,* 220020−220029.

(22) Sun, R. P.; Cubaud, T. Dissolution of carbon dioxide bubbles and microfluidic multiphase flows. *Lab Chip* **2011,** *11*(17)*,* 2924−2928.

(23) Abolhasani, M.; Singh, M.; Kumacheva, E.; Günther, A. Automated microfluidic platform for studies of carbon dioxide dissolution and solubility in physical solvents. *Lab Chip* **2012,** *12*(9)*,* 1611−1618.

(24) Tan, J.; Lv− Y. C.; Xu, J. H.; Luo, G. S. Mass transfer performance of gas-liquid segmented flow in microchannels. *Chem. Eng. J.* **2012,** *181−182,* 229−235.

(25) Yao, C. Q.; Dong, Z. Y.; Zhao, Y. C.; Chen, G. W. An online method to measure mass transfer of slug flow in a microchannel. *Chem. Eng. Sci.* **2014,** *112,* 15−24.

(26) Zhu, C. Y.; Li, C. F.; Gao, X. Q.; Ma, Y. G.; Liu, D. Z. Taylor flow and mass transfer of CO_2 chemical absorption into MEA aqueous solutions in a T-junction microchannel. *Int. J. Heat Mass Transfer.* **2014,** *73*(7)*,* 492−499.

(27) Zhu, C. Y.; Lu, Y. T.; Fu, T. T.; Ma, Y. G.; Li, H. Z. Experimental investigation on gas-liquid mass transfer with fast chemical reaction in microchannel. *Int. J. Heat Mass Transfer* **2017,** *114,* 83−89.

(28) Caplow, M. Kinetics of carbamate formation and breakdown. *J. Am. Chem. Soc.* **1968,** *90,* 6795−6803.

(29) Danckwerts, P. V. The reaction of CO_2 with ethanolamines. *Chem. Eng. Sci.* **1979,** *34*(4)*,* 443−446.

(30) Crooks, J. E.; Donnellan, J. P. Kinetics and mechanism of the reaction between carbon dioxide and amines in aqueous solution. *J. Chem. Soc. Perkin Trans.* **1989,** *2*(4)*,* 331−333.

(31) da Silva, E. F.; Svendsen, H. F. Ab initio study of the reaction of carbamate formation from CO_2 and alkanolamines. *Ind. Eng. Chem. Res.* **2004,** *43*(13)*,* 3413−3418.

(32) Hagewiesche, D. P.; Ashour, S. S.; Al-Ghawas, H. A.; Sandall, O. C. Absorption of carbon dioxide into aqueous blend of monoethanolamine and N-methyldiethanolamine. *Chem. Eng. Sci.* **1995,** *50*(7)*,* 1071−1079.

(33) Horng, S. Y.; Li, M. H. Kinetics of absorption of carbon dioxide into aqueous solutions of monoethanolamine + Triethanolamine. *Ind. Eng. Chem. Res.* **2002,** *41*(2)*,* 257−266.

(34) Blauwhoff, P. M. M.; Versteeg, G. F.; Van Swaaij, W. P. M. A study on the reaction between CO_2 and alkanolamines in aqueous solutions. *Chem. Eng. Sci.* **1984,** *39*(2), 207−225.

(35) Ying, J. R.; Eimer, D. A. Measurements and correlations of diffusivities of nitrous oxide and carbon dioxide in monoethanolamine + water by laminar liquid jet. *Ind. Eng. Chem. Res.* **2012**, 51, 16517−16524.

(36) van Krevelen, D. W; Hoftijzer, P. J. Kinetics of gas-liquid reactions part I. General theory. *Recl. Trav. Chim. Pays-Bas.* **1948,** *67*(7)*,* 563−586.

34

(37) Clarke, J. K. A. Kinetics of absorption of cardon dioxide in monoethanolamine solutions at short contact times. *Ind. Eng. Chem. Fund.* **1964,** *3*(3)*,* 239−245.

(38) Browning, G. J.; Weiland, R. H. Physical solubility of carbon dioxide in aqueous alkanolamines via nitrous oxide analogy. *J. Chem. Eng. Data* **1994,** *39*(4)*,* 817−822.

(39) Diab, F.; Provost, E.; Laloue, N.; Alix, P.; Souchon, V.; Delpoux, O.; Fürst, W. Quantitative analysis of the liquid phase by FT-IR spectroscopy in the system CO_2/diethanolamine (DEA)/H_2O. *Fluid Phase Equilibr.* **2012,** *325,* 90−99.

(40) Chen, Q.; Balaji, S. P.; Ramdin, M.; Gutierrez-Sevillano, J. J.; Bardow, A.; Goetheer, E.; Vlugt, T. J. H. Validation of the CO_2/N_2O analogy using molecular simulation. *Ind. Eng. Chem. Res.* **2014,** *53*(46)*,* 18081−18090.

(41) Hartono, A.; Mba, E. O.; Svendsen, H. F. Physical properties of partially CO_2 loaded aqueous monoethanolamine (MEA). *J. Chem. Eng. Data* **2014,** *59*(6)*,* 1808−1816.

(42) Versteeg, G. F.; van Swaaij, W. P. M. Solubility and diffusivity of acid gases (CO_2, N_2O) in aqueous alkanolamine solutions. *J. Chem. Eng. Data* **1988,** *33*(1)*,* 29−34.

(43) Kasturi, G.; Stepanek, J. B. Two-phase flow—IV. Gas and liquid side mass transfer coefficients. *Chem. Eng. Sci.* **1974**, *29,* 1849−1856.

(44) Yao, C. Q.; Dong, Z. Y.; Zhang, Y. C.; Mi, Y.; Zhao, Y. C.; Chen, G. W. On the leakage flow around gas bubbles in slug flow in a microchannel. *AIChE J.* **2015,** *61*(11)*,* 3964−3972.

(45) Aussillous, P.; Quéré, D. Quick deposition of a fluid on the wall of a tube. *Phys. Fluids* **2000,** *12*(10)*,* 2367−2371.

(46) Vázquez, G.; Alvarez, E.; Navaza, J. M.; Rendo, R.; Romero, E. Surface Tension of Binary Mixtures of Water + Monoethanolamine and Water + 2-Amino-2-methyl-1-propanol and Tertiary Mixtures of These Amines with Water from 25 to 50 $^{\circ}$C. *J. Chem. Eng. Data* **1997,** *42*(1)*,* 57−59.

(47) Shim, S.; Wan, J.; Hilgenfeldt, S.; Panchal, P. D.; Stone, H. A. Dissolution without disappearing: multicomponent gas exchange for CO_2 bubbles in a microfluidic channel. *Lab Chip* **2014,** *14*(14)*,* 2428−2436.

(48) Dang, M. H.; Yue, J.; Chen, G. W.; Yuan, Q. Formation characteristics of Taylor bubbles in a microchannel with a converging shape mixing junction. *Chem. Eng. J.* **2013,** *223,* 99−109.

(49) Tan, J.; Lv, Y. C.; Xu, J. H.; Luo, G. S. Mass transfer characteristic in the formation stage of gas-liquid segmented flow in microchannel. *Chem. Eng. J.* **2012**, *185−186,* 314−320.

(50) Hikita, H.; Asai, S.; Ishikawa, H.; Honda, M. The kinetics of reactions of carbon dioxide with monoethanolamine, diethanolamine and triethanolamine by a rapid mixing method. *Chem. Eng. J.* **1977**, *13*, 7−12.

(51) Santiago, M.D.; Farina, I.H. Mass transfer with second order reaction-numerical solution. *Chem. Eng. Sci.* **1970,** *25,* 744−747.

(52) Butler, C.; Lalanne, B.; Sandmann, K.; Cid, E.; Billet, A. M. Mass transfer in Taylor flow: transfer rate modelling from measurements at the slug and film scale. *Int. J. Multiphase Flow* **2018,** *105,* 185−201.

(53) Incropera, F. P.; DeWitt, D. P. Fundamentals of heat and mass transfer; Wiley, USA, **2002**.

(54) Das, S. Fundamentals of heat and mass transfer; Alpha Science International Ltd., UK, **2010.**